DOI: 10.13009/EUCASS2017-212



# Numerical Analysis of Acoustic Loads Generated by Supersonic Jets

Seong Ryong Koh[*†], Andreas Henze[*], Matthias Meinke[*,a], Wolfgang Schröder[*,a]
[*]*Institute of Aerodynamics, RWTH Aachen University, Wüllnerstraße 5a, 52062 Aachen, Germany*
[a]*JARA – High-Performance Computing, Forschungszentrum Jülich, 52425 Jülich, Germany*
s.koh@aia.rwth-aachen.de · a.henze@aia.rwth-aachen.de · m.meinke@aia.rwth-aachen.de · office@aia.rwth-aachen.de
[†]Corresponding author

Hauke Schmidt[b], Athanasios Dafnis[b]
[b]*Institute of Structural Mechanics and Lightweight Design, RWTH Aachen University*
*Wüllnerstraße 7, 52062 Aachen, Germany*
hauke.schmidt@sla.rwth-aachen.de · athanasios.dafnis@sla.rwth-aachen.de

## Abstract

A hybrid computational fluid dynamics (CFD) and computational aeroacoustics (CAA) method is used to compute the flow and the acoustic field of supersonic jets at a Mach number of 3.6. The flow simulations are performed by highly resolved large-eddy simulations (LES) from which sound source terms are extracted to compute the acoustic field by solving the acoustic perturbations equations (APE). The acoustic loads are determined on the structural components to obtain the correct dynamic behavior of non-rigid surfaces at atmospheric flight conditions using fluid-structure interaction (FSI) methods.

## Introduction

The tailored design of Expendable Launch Vehicle (ELV) with large flexible components like the fairing is strongly affected by aeroelastic effects and acoustic loads during the launch phase. A large range of vibration and acoustic loads and nonlinearities have to be taken into account in the development and analysis of ELV. Therefore, an efficient computational approach is essential to resolve the physics defined by the various length scales of fluid dynamics, aeroacoustics, and solid mechanics. The relevant scales in the low and high frequency range require an accurate numerical solver of the viscous flow such that the acoustic field can be determined with the high resolution of the near-field of a launcher body. The acoustic loads and the structural vibration can be determined by a dynamic aeroelastic analysis based on a loose coupling method linking the flow field, the acoustic field, and the structural system. Essential issues are to reduce uncertainties in the numerical analysis for an efficient tailored design of ELV applications and to decrease the large safety margins within the specification of acoustic loads on the structural design.

In the present study, the objective is to predict the sound generation and to identify the essential noise sources of the supersonic jets such that the acoustic loads on the structural components can be precisely determined. The high-fidelity solution of acoustic loads enables the structural analysis to obtain the correct dynamic behavior of non-rigid surfaces at atmospheric flight conditions using fluid-structure interaction (FSI) methods. The sound generation and the influence on the structural components are accurately assessed based on a coupled fluid mechanics and aeroacoustics analysis. The turbulent flow problem in the supersonic regime is analyzed by a two-step analysis consisting of a large-eddy simulation (LES) to determine the flow field and of solutions of the acoustic perturbation equations (APE) to investigate the acoustic field. To ensure a high-efficiency of the integrated numerical procedure, the discrete Fourier modes and the full broadband acoustic signal are determined by the computational aeroacoustics (CAA) approach. In addition to the prediction of the noise generation, the unsteady flow solutions determined by the LES also enable a more detailed analysis of the noise sources.

DOI: 10.13009/EUCASS2017-212



## Numerical Method

### Flow and acoustic solver

The Navier-Stokes equations for three-dimensional unsteady compressible flow are solved by a large-eddy simulation (LES) formulation using the monotone integrated LES (MILES) approach.[4] The discretization of the inviscid terms consists of a mixed centered-upwind advective upstream splitting method (AUSM) scheme at second-order accuracy and the viscous terms are discretized using a second-order accurate centered approximation. The temporal integration is done by a second-order explicit 5-stage Runge-Kutta method. A detailed description of the fundamental flow solver is given in[9] and the quality of its solutions in turbulent jets is thoroughly discussed in.[2,8]

The equations describing the sound propagation are the acoustic perturbation equations (APE) in the APE-4 formulation[3] whose acoustic sources are determined by the compressible LES. The acoustic perturbation equations were derived from the continuity and Navier-Stokes equations. Using an expression for the excess density $\rho_e = (\rho - \overline{\rho}) - (p - \overline{p})/\overline{a^2}$, where the overbar denotes mean quantities, the rearranged APE-4 system[7] reads

$$\frac{\partial p'}{\partial t} + \overline{a^2}\nabla \cdot \left(\overline{\rho}\mathbf{u}' + \overline{\mathbf{u}}\,\frac{p'}{\overline{a^2}}\right) = \overline{a^2}(q_c + q_e) \tag{1}$$

$$\frac{\partial \mathbf{u}'}{\partial t} + \nabla\left(\overline{\mathbf{u}} \cdot \mathbf{u}'\right) + \nabla\left(\frac{p'}{\overline{\rho}}\right) = \mathbf{q}_m \quad . \tag{2}$$

The right-hand side source terms are

$$q_c = -\nabla \cdot (\rho'\mathbf{u}')' \ , \tag{3}$$

$$q_e = -\frac{\partial \rho_e}{\partial t} - \nabla \cdot (\rho_e \overline{\mathbf{u}}) \ , \tag{4}$$

$$\mathbf{q}_m = -(\omega \times \mathbf{u})' - \left(\nabla \frac{|\mathbf{u}'|^2}{2}\right)' + \nabla \frac{p'}{\overline{\rho}} - \left(\frac{\nabla p}{\rho}\right)' . \tag{5}$$

The excess density represents the difference between the density and the pressure perturbation at an analogous acoustic medium whose density perturbation is isentropic and the sound speed is $a$. The first step of the hybrid method is based on an LES for the turbulent jet flow to provide the data of the noise source terms Eqs. (3), (4), and (5). Then, the corresponding acoustic field is computed by solving the acoustic perturbation equations (1) and (2).

To accurately resolve the acoustic wave propagation described by the acoustic perturbation equations in the APE-4 formulation[7] a sixth-order dispersion-relation-preserving finite difference scheme[12] is used for the spatial discretization and an alternating 5-6 stage low-dispersion and low-dissipation Runge-Kutta method for the temporal integration.[5] On the embedded boundaries between the inhomogeneous and the homogeneous acoustic domain an artificial damping zone has been implemented to suppress spurious sound generated by the acoustic-flow-domain transition.[10] A detailed description of the two-step method and the discretization of the Navier-Stokes equations and the acoustic perturbation equations is given in.[3] For the acoustic computations, non-reflecting boundary conditions[12] are prescribed on the boundaries of the computational domain.

### Flow condition

The supersonic jet is configured by the stagnation temperature $T_{j0}$ = 3500K and the stagnation pressure $P_{j0}$ = 84.34bar which result in the nozzle exit Mach number $M_j$ = 3.6 and the corresponding jet speed $U_j$ is 2541.3m/s. The jet Reynolds number based on the nozzle diameter $D = 2R$ is approx. $15.62 \times 10^6$ where the jet plume viscosity is determined by Sutherland's law. The ambient flow conditions are defined by three Mach numbers at a low and a high altitude. The ambient flow speed $U_a$ is calculated by the ambient Mach number $M_a$ and the speed of sound $c_a$ at each atmospheric condition. The Reynolds number based on the nozzle exit diameter $Re = \rho_a U_a D/\mu_a$ is $22.57 \times 10^6$ at $M_a = 0.72$.

## Results

### Mean main body and nozzle flow

The ambient flow condition is configured to determine the acoustic generation of an overexpanded jet flow at the freestream Mach number of 0.5. The mean flow obtained by solving the Reynolds-averaged Navier-Stokes (RANS)

DOI: 10.13009/EUCASS2017-212



equations is shown in Fig. 1. The pressure contours in Figs. 1(a) and (b) show a smooth variation in the external flow over the main launcher body. In the nozzle exit region in Fig. 1(a) a shock occurs in the supersonic jet. The radial pressure distribution in Fig. 1(c) is obtained right in the nozzle exit. The pressure outside the nozzle is much higher than the mean pressure distribution of the jet at the nozzle exit, i.e., an overexpanded jet is computed.

The inflow condition of the supersonic jet is based on the mean flow field shown in Fig. 2. The values at the nozzle exit match the data based on the algebraic formulation of the converging-diverging nozzle which yields for the exit temperature $T_j$=1718.4K and the exit static pressure $P_j$=485.47 mbar. The turbulence intensity in Fig. 2(d) shows a large increase on the centerline ($r = 0$) and a peak near the nozzle wall ($r \simeq 1.16$ m).

## Analysis of the supersonic jets

The supersonic jet is analyzed based on large-eddy simulations using the inflow condition obtained by the RANS solution. To generate a turbulent transition, an artificial vortex ring is imposed near the nozzle exit. In the present analysis, a forcing introduced by Bogey et al.[1] is imposed to ensure a physically modeled transition. The inflow forcing is controlled to generate proper turbulence using the grid size and the random azimuthal modes distributed over the vortex ring.

The contours of the density gradient and the axial velocity components are presented in Fig. 3. In general, the near field possesses three characteristic wave patterns which are represented by the density gradient contours. The primary Mach waves propagate downstream at a certain polar angle in the range of 30deg. Moreover, sideline waves occur due to the turbulent mixing of the jet. Furthermore, the instability waves interacting with the shear layer propagate upstream. The intensity of the upstream waves is intensified by lowering the freestream Mach number. The contours of the axial velocity component in Figs. 3(c) and (d) show that the jet development of the underexpanded jets results in a larger convection speed near the centerline compared to the overexpanded jets.

In the following, the mean axial velocity profiles are compared, i.e., the development of the shear layer and the distribution of the turbulence intensities are considered. The sampling time period is $T_{\text{sample}} = 140R/U_\infty$ at a time step $\Delta t_{\text{sample}} = 0.05R/U_\infty$ such that 2800 LES snapshots are averaged. The time-averaged flow field in Fig. 4 shows the coherent shock structures inside the supersonic jets. The mean axial velocity is illustrated in the $y > 0$ plane and the mean density in the $y < 0$ plane. The jet diameter in the downstream direction varies due to the different nozzle exit conditions which influence the shock structure and the mean convection speed near the centerline.

In Fig. 5 the profiles of the mean axial velocity normalized by the nozzle exit velocity $U_j$ show the flow development on the jet centerline. The streamwise location of the first shock is $z/R = 2$ for the overexpanded jets and $z/R = 3$ for the underexpanded jets. The shock cell size increases from $5R$ for the overexpanded jets to $7R$ for the underexpanded jets. In the jet's near field three strong shocks occur. Then, further downstream of the strong shocks, the mean axial velocity decreases at a constant rate to the axial distance. The velocity magnitude of the underexpanded jets is 66% larger at $z/R = 30$ than that of the overexpanded configuration.

The distribution of the turbulence intensity is presented in Fig. 6. The turbulent fluctuations near the shear layer (right column) are much larger than those on the centerline (left column). All distributions develop the peak turbulence intensity downstream of the first shock near the shear layer. For the overexpanded jets in Figs. 6(a) and (b) the turbulent fluctuations on the centerline rise rapidly and peak downstream of the initial region. The centerline distribution of the underexpanded jet in Figs. 6(c) and (d) shows a smoother increase of the turbulence intensity since the shocks are weak such that a smooth jet development with small nonlinear effects is observed. The nonlinear development of the jets leads to a rapid increase of the turbulence intensities in the near field. Downstream of the initial region almost similar velocity fluctuations occur. The turbulence intensities are hardly impacted by varying the freestream Mach number.

The mean pressure contours and the overall sound pressure level (OASPL) are presented in Fig. 7. The pressure contours shown in the $y > 0$ domain evidence the shock structure inside the supersonic jets. The OASPL near the jet region is massively increased by the nozzle exit condition, i.e., the overexpanded jets generate more powerful waves. The freestream Mach number also possesses a serious impact on the pressure fluctuations in the jet near-field. At $y/R = 10$ and $z/R = 5$, i.e., 'P1' in Figs. 7(a) and (b), the OASPL is 142.4dB at the freestream Mach number 0.5 and 137.2dB at the freestream Mach number 0.72. The same acoustic attenuation is reached by doubling the microphone distance from the acoustic source. As shown in Fig. 3 the instability waves moving upstream appear over the complete axial extent of the jet ($z/R \leq 40$). Nevertheless, assuming a compact source located at $z/R = 20$ on the jet centerline, where the turbulence intensity peak occurs, the OASPL on the main launcher body can be estimated based on the acoustic pressure relationship with the microphone distance $r_m$, e.g., the microphone distance of 'P1' is approx. $18R$. For the freestream Mach number 0.5, the OASPL on the payload fairing ($r_m \simeq 36R$) is 136.4dB (6dB attenuation). According to the 2014 Vega user's manual (page 3-6) the design limit under the payload fairing is OASPL 133.7dB at atmospheric conditions.

DOI: 10.13009/EUCASS2017-212



**Sound source near the jet nozzle**

The unsteady data determined by the LES are used to calculate the acoustic loads on the payload fairing. The pressure contours in Fig. 8 are obtained by the current LES at the freestream Mach number 0.5. The eddy convection inside the jet is illustrated by the density distributions in Figs. 9(a) and (b). The density distributions in Fig. 9(c) are determined at the radial distance $r = 5R$ from the centerline. The figures represent the time-dependent variation in the streamwise direction ($0 \leq z/R \leq 38$) at the fixed radial coordinate of $r/R = 0$, 1, and 5. The dashed line in Figs. 9(a) and (b) indicates the ambient speed of sound in the downstream direction. In Fig. 9(c) the dashed line illustrates the convection to the upstream at 50% of the ambient speed of sound. On the centerline ($r/R = 0$), the shock structures appear with the eddy fluctuations convecting at supersonic speed. The contours near the shear layer $r/R = 1$ include the supersonic eddy convection due to the jet development in the axial direction. Since the strong wave generation occurs in the supersonic turbulent jet, the acoustic field in the subsonic regime consists of the linear acoustic propagation and the Mach waves possessing nonlinear acoustic dissipation. In Fig. 9(c), the instability waves exist in the range $10 \leq z/R \leq 38$ where the strong downstream Mach waves are superposed with the instability waves. Upstream of the region $z/R \leq 10$ the instability waves propagate to the main launcher body.

The pressure signals obtained by the LES are presented in Fig. 10. The non-dimensional time scale is compared with the period of 100Hz and 500Hz signals. Near the shear layer, the small scale eddies moving at high frequencies over 500Hz contribute to the pressure fluctuations in Fig. 10(a). Between the first and the second shock at $z/R = 4$, strong pressure fluctuations occur at $2R/U_\infty$, $4.5R/U_\infty$, and $6R/U_\infty$. The pressure signals in Fig. 10(b) are obtained at the radial coordinate $r/R = 5$ to observe the instability waves only. The interaction between the shear layer and the instability waves generates the jet screech. The wave propagation to the upstream direction excites the shear layer near the nozzle exit such that a feedback mechanism sustains the strong aerodynamic oscillation usually accompanied by its harmonics. The first harmonics possess the frequency range $0.05 \leq fD/U_j \leq 0.2$ such that Tam et al.[11] found the fundamental screech tone valid for hot and cold jets

$$\frac{fD}{U_j} = \frac{0.67}{\sqrt{M_j^2 - 1}} \left[ 1 + \frac{0.7\ M_j}{\sqrt{1 + \frac{\gamma - 1}{2} M_j^2}} \left( \frac{T_j}{T_{j0}} \right)^{-1/2} \right]^{-1} .$$

Based on this semi-empirical model the acoustic pressure signal of the present supersonic jet is determined up to the 5th harmonic of the fundamental screech tone in Fig. 11(a). The amplitudes of the pressure fluctuations are determined based on the overall sound pressure level in Fig. 7. The corresponding power spectrum is presented in Fig. 11(b). The first harmonic is located at the frequency of $fD/U_j \approx 0.1$ (100Hz).

To compute the preloaded state of the payload fairing (PLF) the stationary structural deformations are determined with respect to the flow condition. Based on the assumption of ideal pressure compensation of the PLF cavity the computation of the structural deformation assumes the inner pressure to be the ambient pressure.

The structural deformations are presented in Fig. 12. The PLF is impacted by the compression due to the dynamic pressure at the top of the PLF. The maximum deformation is observed in the center cylindrical part of the PLF at Mach number $M_a$=0.9, where the shells of the PLF bulge outward by up to 0.156 mm due to the lower pressure. The deformations are symmetric with respect to the separation plane of the PLF. In Fig. 13 the mode shapes of a dynamic preload at the frequency 92.8Hz is presented for the PLF at the ambient Mach numbers 0.72 and 0.9 at the altitude of 6km. Increasing the Mach number the dynamic pressure on the PLF significantly shifts the deformation to higher mode.

## Summary

A hybrid computational fluid dynamics (CFD) and computational aeroacoustics (CAA) method is used to compute the flow and the acoustic field of supersonic jets at a Reynolds number approx. 16 million and a Mach number of 3.6. The flow simulations are performed by highly resolved large-eddy simulations (LES) from which sound source terms are extracted to compute the acoustic field by solving the acoustic perturbations equations (APE).

The near field possesses three characteristic wave patterns, i.e., Mach waves, sideline waves, and instability waves. The primary Mach waves propagate downstream at a polar angle in the range of 30deg. The sideline waves occur due to the turbulent mixing of the jet. Furthermore, the instability waves interacting with the shear layer propagate upstream. The intensity of the upstream waves is intensified by lowering the freestream Mach number. Since the strong wave generation occurs in the supersonic turbulent jet, the acoustic field in the subsonic regime consists of the linear acoustic propagation and the Mach waves possessing nonlinear acoustic dissipation. The instability waves exist over the axial coordinates $10 \leq z/R \leq 38$ where the strong downstream Mach waves are superposed with the instability waves. Upstream of the region $z/R \leq 10$ the instability waves propagate to the main launcher body. Based on a

DOI: 10.13009/EUCASS2017-212



semi-empirical model the acoustic pressure signal of the present supersonic jet is determined up to the 5th harmonic of the fundamental screech tone. The dynamic preload analysis shows that the structural deformation is shifted to higher modes by increasing the ambient Mach number.

## Acknowledgments

The authors gratefully acknowledge the Gauss Centre for Supercomputing (GCS) for providing computing time for a GCS Large-Scale Project on the GCS share of the supercomputer Hazelhen at HLRS Stuttgart and JUQUEEN[6] at Jülich Supercomputing Centre (JSC). GCS is the alliance of the three national supercomputing centres HLRS (Universität Stuttgart), JSC (Forschungszentrum Jülich), and LRZ (Bayerische Akademie der Wissenschaften), funded by the German Federal Ministry of Education and Research (BMBF) and the German State Ministries for Research of Baden-Württemberg (MWK), Bayern (StMWFK), and Nordrhein-Westfalen (MIWF).

## References

[1] C. Bogey, O. Marsden, and C. Bailly. Large-eddy simulation of the flow and acoustic fields of a Reynolds number $10^5$ subsonic jet with tripped exit boundary layers. *Phys. Fluids*, 23(3):035104, 2011.

[2] M. O. Cetin, S. R. Koh, M. Meinke, and W. Schröder. Numerical analysis of the impact of the interior nozzle geometry on low mach number jet acoustics. *Flow Turbul. Combust.*, 98(2):417–443, 2017.

[3] R Ewert and W Schröder. Acoustic perturbation equations based on flow decomposition via source filtering. *J. Comput. Phys.*, 188(2):365–398, 2003.

[4] C. Fureby and F. Grinstein. Monotonically integrated large eddy simulation of free shear flows. *AIAA J.*, 37:544–556, 1999.

[5] F Q Hu, M Y Hussaini, and J L Manthey. Low-dissipation and low-dispersion Runge-Kutta schemes for computational acoustics. *J. Comput. Phys.*, 124(1):177–191, 1996.

[6] Jülich Supercomputing Centre. JUQUEEN: IBM Blue Gene/Q Supercomputer system at the jülich supercomputing centre. *J. Large-Scale Research Facilities*, 1(A1), 2015.

[7] S. R. Koh, G. Geiser, and W. Schröder. Reformulation of acoustic entropy source terms. *AIAA Paper*, 2011-2927, 2011.

[8] S. R. Koh, W. Schröder, and M. Meinke. Turbulence and heat excited noise sources in single and coaxial jets. *J. Sound Vib.*, 329:786–803, 2010.

[9] M. Meinke, W. Schröder, E. Krause, and Th. Rister. A comparison of second- and sixth-order methods for large-eddy simulations. *Comput. Fluids*, 31(4):695–718, 2002.

[10] W. Schröder and R. Ewert. Some concepts of LES-CAA coupling. In C. Wagner, T. Hüttl, and P. Sagaut, editors, *Large-Eddy Simulations for Acoustics*, pages 222–237. Cambridge University Press, 2007.

[11] C. K. W. Tam, J. M. Seiner, and J. C. Yu. Proposed relationship between broadband shock associated noise and screech tones. *J. Sound Vib.*, 110:309–321, 1986.

[12] C. K. W. Tam and J. C. Webb. Dispersion-relation-preserving finite difference schemes for computational acoustics. *J. Comput. Phys.*, 107(2):262–281, 1993.

DOI: 10.13009/EUCASS2017-212



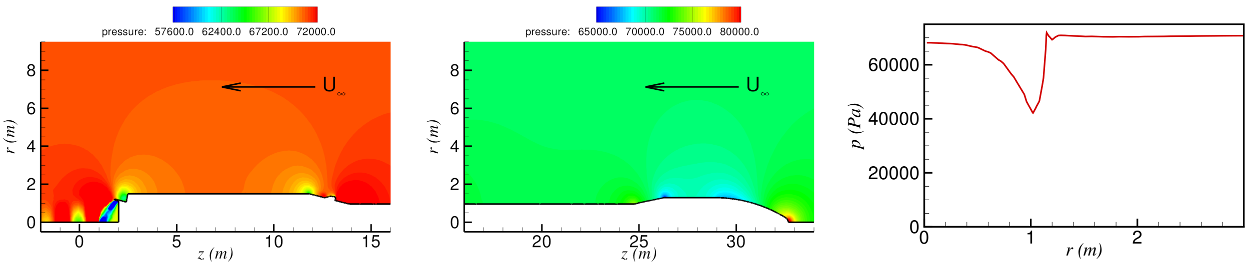


(a) (b) (c)

Figure 1: Contours of the mean flow field around the main body determined by the RANS computation where the flow direction is from right to left; (a) nozzle, (b) payload region, and (c) radial pressure distribution at the nozzle exit.

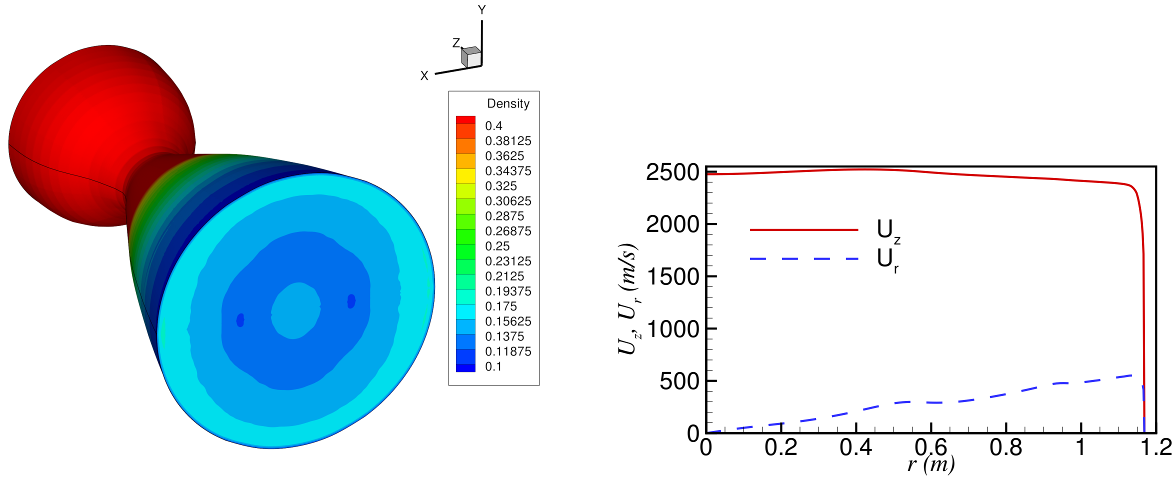


(a) (b)

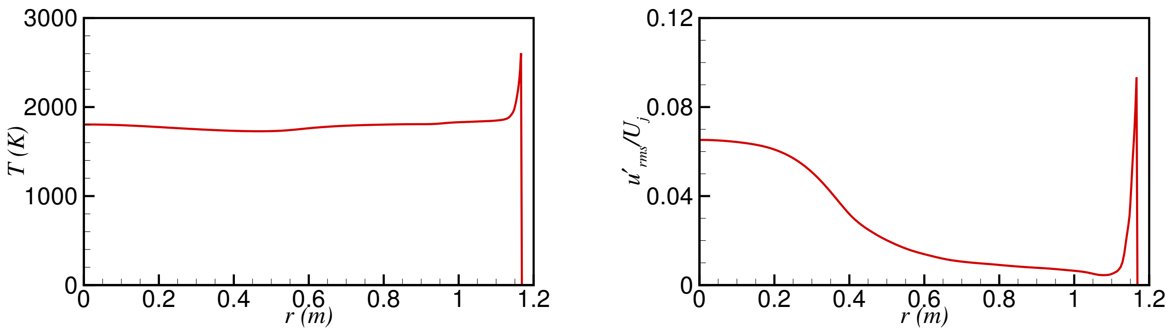


(c) (d)

Figure 2: Mean flow field at the exit the nozzle determined by the RANS computation; (a) density contours, (b) profiles of the axial (solid line) and radial (dashed line) velocity component, (c) temperature distribution, and (d) turbulence intensity distribution.

DOI: 10.13009/EUCASS2017-212



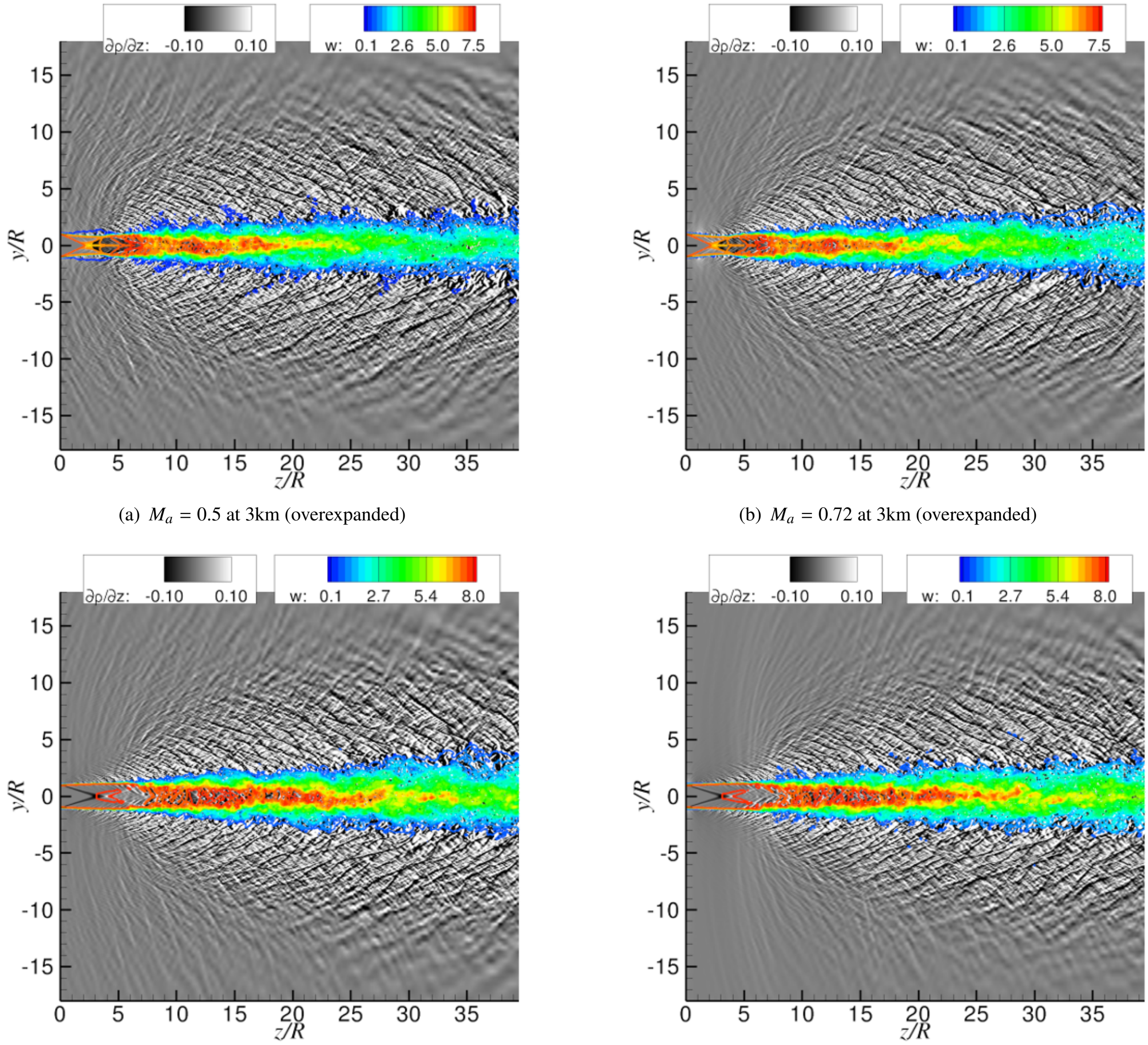


(a) $M_a = 0.5$ at 3km (overexpanded)

(b) $M_a = 0.72$ at 3km (overexpanded)

(c) $M_a = 0.72$ at 6km (underexpanded)

(d) $M_a = 0.9$ at 6km (underexpanded)

Figure 3: Contours of the density gradient in the axial direction ($\partial\rho/\partial z$) and the axial velocity component ($w$).

DOI: 10.13009/EUCASS2017-212



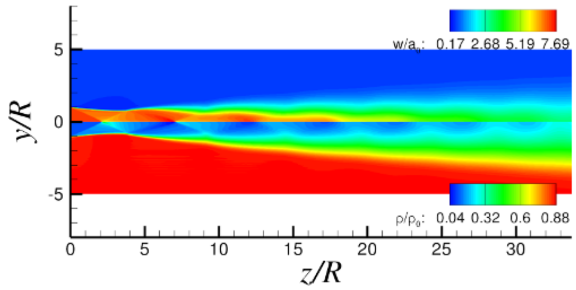


(a) $M_a$ = 0.5 at 3km (overexpanded)

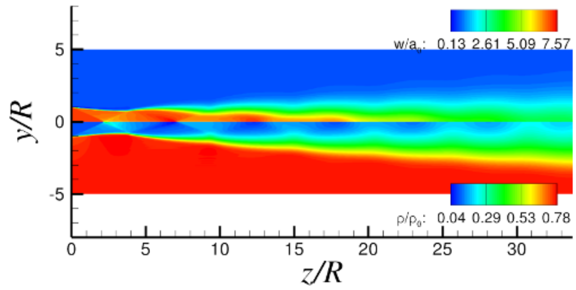


(b) $M_a$ = 0.72 at 3km (overexpanded)

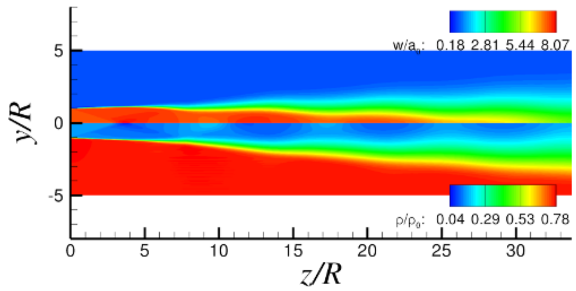


(c) $M_a$ = 0.72 at 6km (underexpanded)

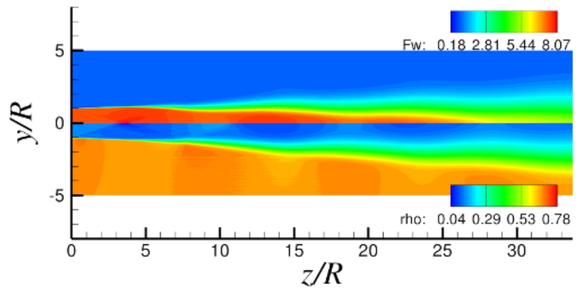


(d) $M_a$ = 0.9 at 6km (underexpanded)

Figure 4: Mean contours of the axial velocity component and the density at several freestream Mach numbers.

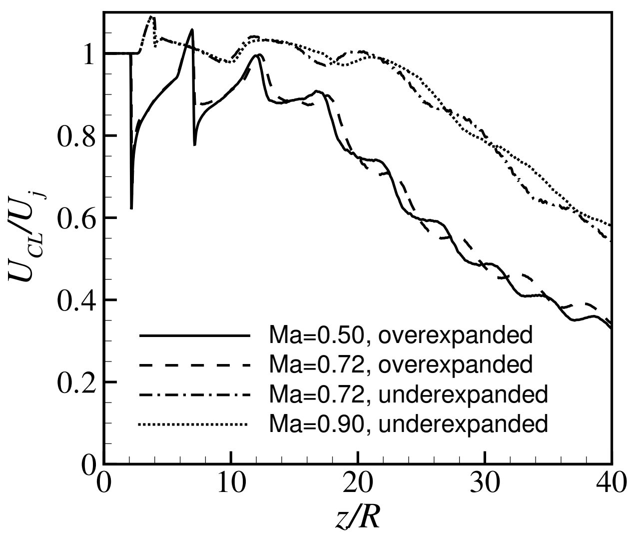


Figure 5: Profiles of the axial velocity component on the centerline.

DOI: 10.13009/EUCASS2017-212



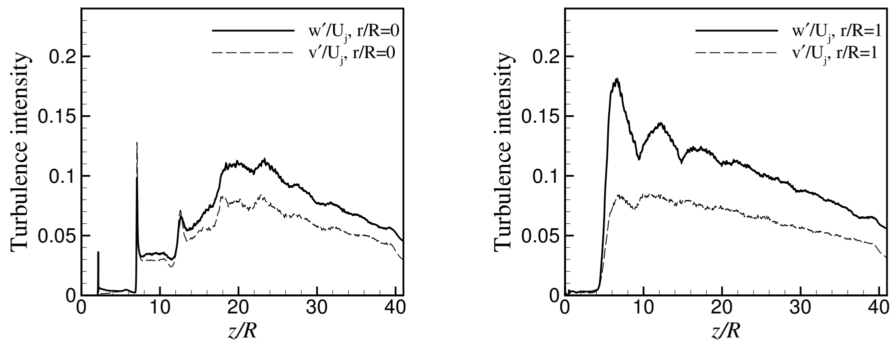


(a) $M_a$ = 0.5 at 3km (overexpanded)

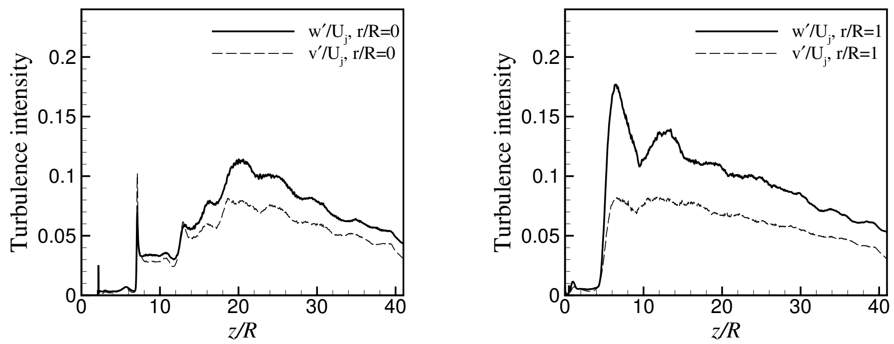


(b) $M_a$ = 0.72 at 3km (overexpanded)

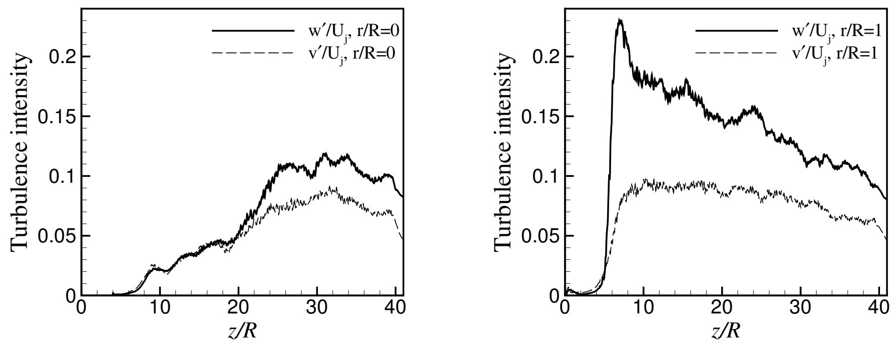


(c) $M_a$ = 0.72 at 6km (underexpanded)

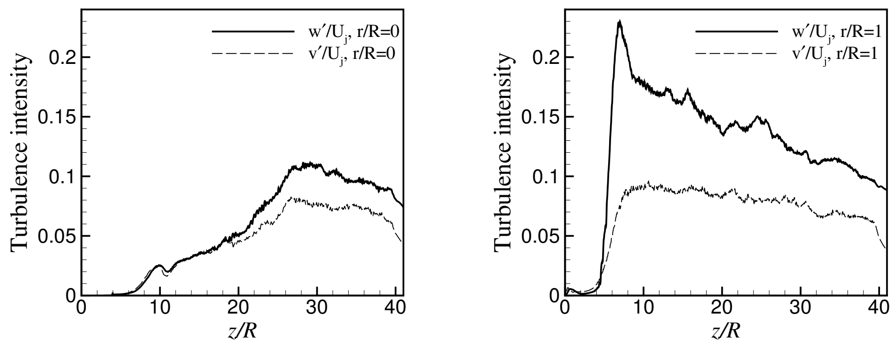


(d) $M_a$ = 0.9 at 6km (underexpanded)

Figure 6: Axial distribution of the turbulence intensity at several freestream Mach numbers.

DOI: 10.13009/EUCASS2017-212



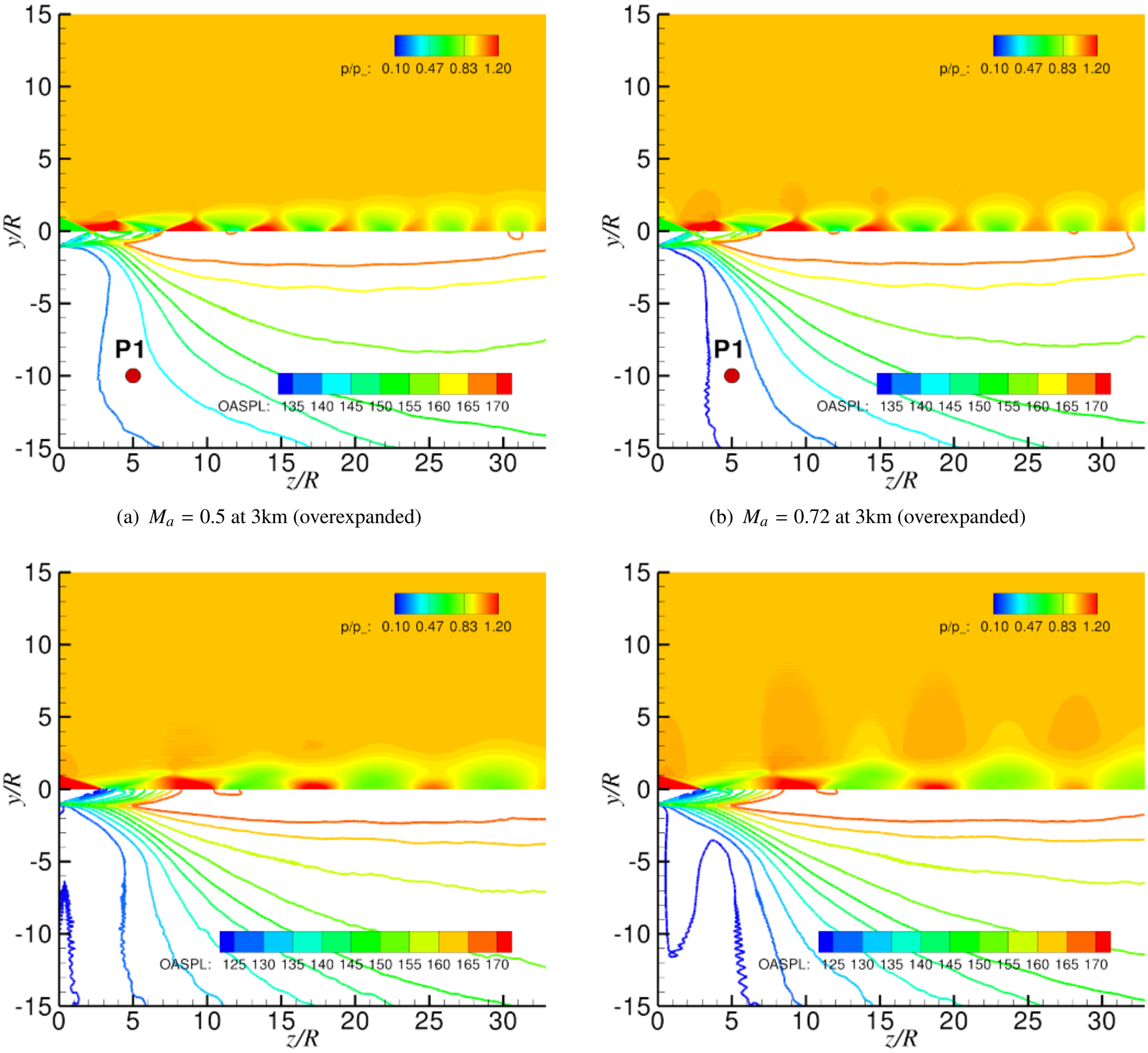


(a) $M_a$ = 0.5 at 3km (overexpanded)

(b) $M_a$ = 0.72 at 3km (overexpanded)

(c) $M_a$ = 0.72 at 6km (underexpanded)

(d) $M_a$ = 0.9 at 6km (underexpanded)

Figure 7: Mean static pressure contours and overall sound pressure level at several freestream Mach numbers.

DOI: 10.13009/EUCASS2017-212



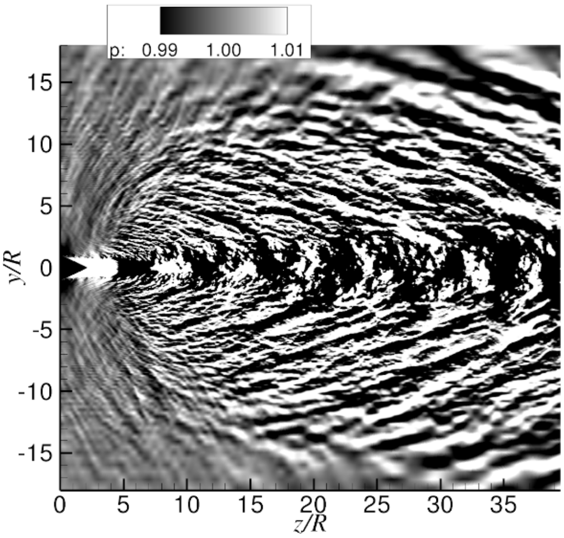


Figure 8: Contours of the pressure fluctuations at the freestream Mach number 0.5.

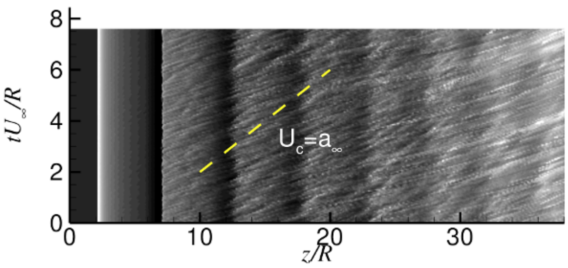


(a) $r = 0$

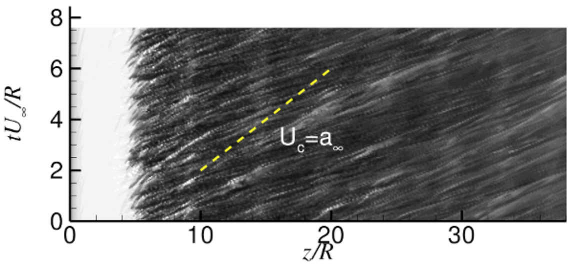


(b) $r/R = 1$

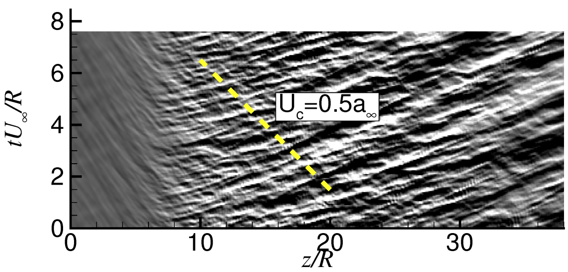


(c) $r/R = 5$

Figure 9: Time-dependent density fluctuations in the axial direction determined for the overexpanded supersonic jet at the freestream Mach number 0.5 at (a) $r/R = 0$, (b) $r/R = 1$, and (c) $r/R = 5$.

DOI: 10.13009/EUCASS2017-212



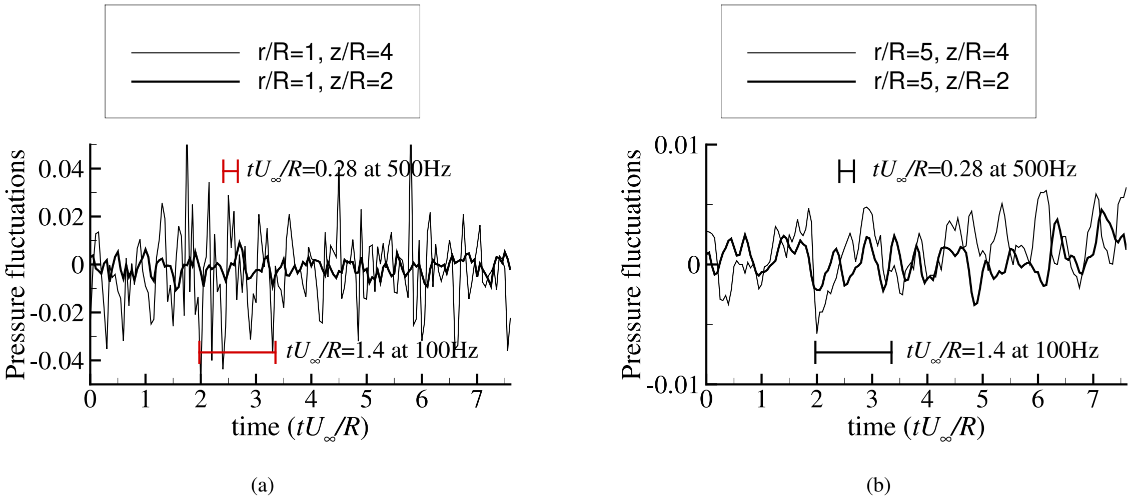


Figure 10: Pressure fluctuations ($p'/\rho_0 a_0^2$) determined for the overexpanded supersonic jet at the freestream Mach number 0.5, (a) pressure signal at $r/R = 1$, (b) pressure signal at $r/R = 5$.

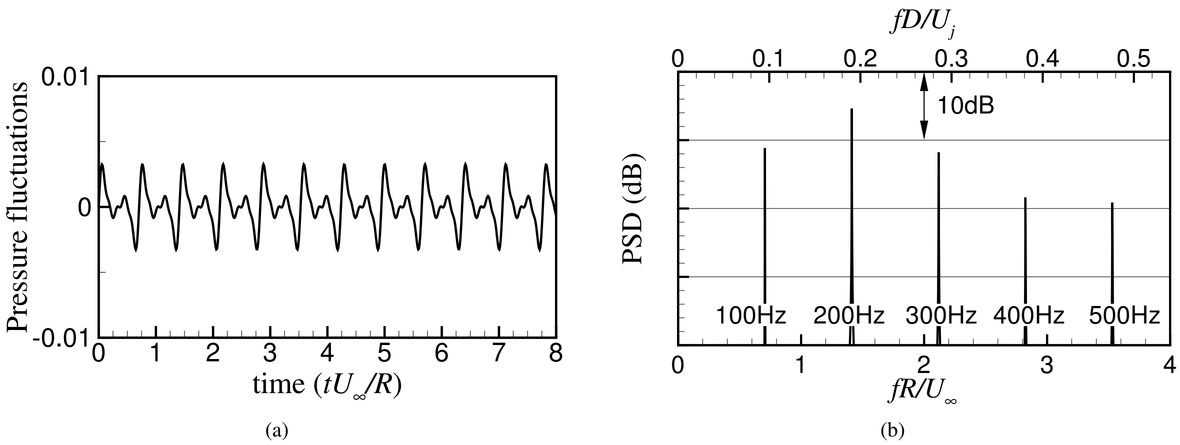


Figure 11: Acoustic pressure signal and the sound spectrum determined by the screech tone model, (a) acoustic pressure signal, (b) sound spectrum.

DOI: 10.13009/EUCASS2017-212



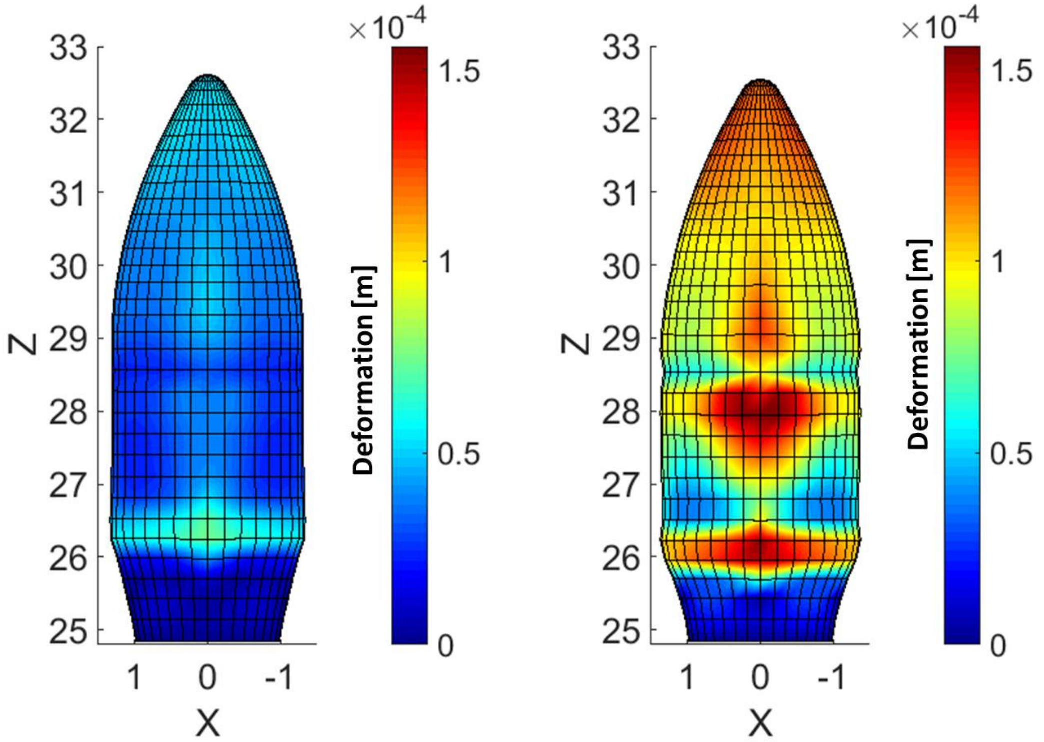


(a) $M_a$ = 0.72 at 6km (underexpanded) (b) $M_a$ = 0.9 at 6km (underexpanded)

Figure 12: Deformation of the payload fairing for the underexpanded jet configuration at the ambient Mach numbers $M_a$=0.72 and $M_a$=0.9.

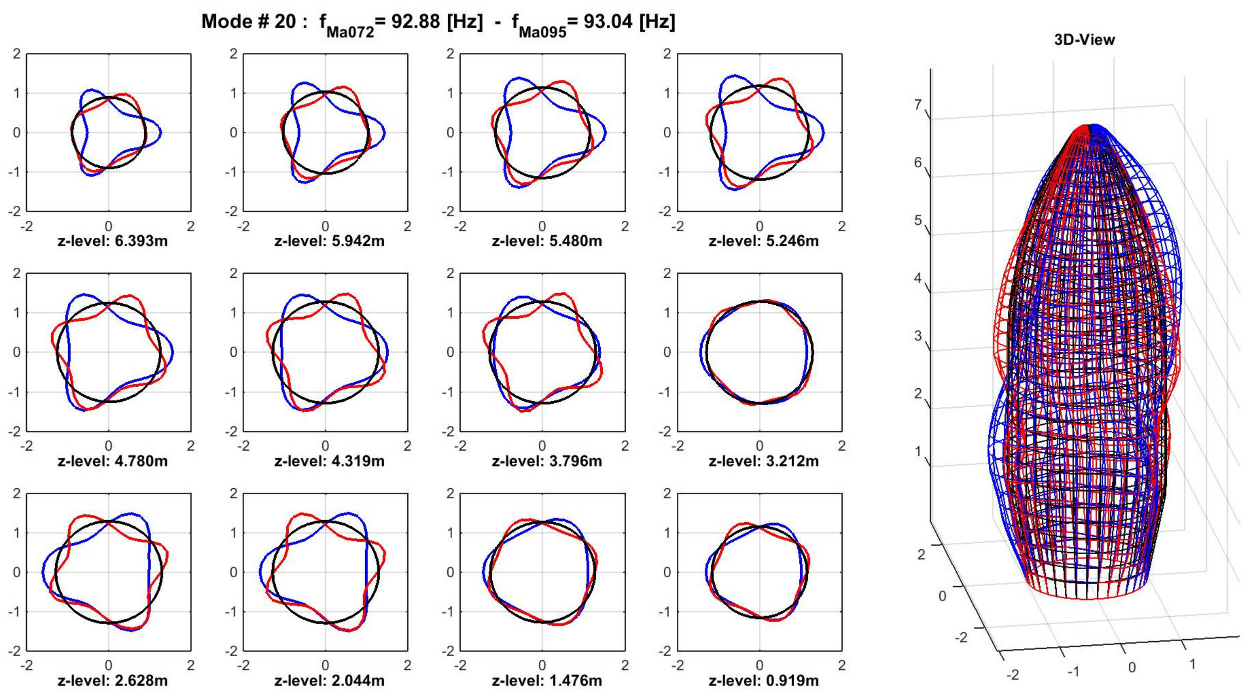


Figure 13: Mode shapes of the preloaded payload fairing at the ambient Mach number $M_a$=0.72 (blue lines) and $M_a$=0.9 (red lines) compared with the original undeformed shape (black lines).